

# Efficient Alkaline Water/Seawater Hydrogen Evolution by a Nanorod-Nanoparticle-Structured Ni-MoN Catalyst with Fast Water-Dissociation Kinetics

Libo Wu, Fanghao Zhang, Shaowei Song, Minghui Ning, Qing Zhu, Jianqing Zhou, Guanhui Gao, Zhaoyang Chen, Qiancheng Zhou, Xinxin Xing, Tian Tong, Yan Yao, Jiming Bao, Luo Yu,\* Shuo Chen,\* and Zhifeng Ren\*

Achieving efficient and durable nonprecious hydrogen evolution reaction (HER) catalysts for scaling up alkaline water/seawater electrolysis is desirable but remains a significant challenge. Here, a heterogeneous Ni-MoN catalyst consisting of Ni and MoN nanoparticles on amorphous MoN nanorods that can sustain large-current-density HER with outstanding performance is demonstrated. The hierarchical nanorod–nanoparticle structure, along with a large surface area and multidimensional boundaries/defects endows the catalyst with abundant active sites. The hydrophilic surface helps to achieve accelerated gas-release capabilities and is effective in preventing catalyst degradation during water electrolysis. Theoretical calculations further prove that the combination of Ni and MoN effectively modulates the electron redistribution at their interface and promotes the sluggish water-dissociation kinetics at the Mo sites. Consequently, this Ni-MoN catalyst requires low overpotentials of 61 and 136 mV to drive current densities of 100 and 1000 mA cm<sup>-2</sup>, respectively, in 1 M KOH and remains stable during operation for 200 h at a constant current density of 100 or 500 mA cm<sup>-2</sup>. This good HER catalyst also works well in alkaline seawater electrolyte and shows outstanding performance toward overall seawater electrolysis with ultralow cell voltages.

## 1. Introduction

Hydrogen is an efficient and clean energy carrier for sustainable energy systems due to its high energy density (142 kJ g<sup>-1</sup>) and pollution-free characteristics.<sup>[1]</sup> Water electrolysis driven by excess renewable energy and/or surplus power from the power grid is an economical and zero-carbon-emission conversion route to produce hydrogen gas that avoids the greenhouse gas emissions from methane in steam-reforming.<sup>[1b,2]</sup> Alkaline water electrolysis is currently more appealing due to its inexpensive equipment requirements and effective avoidance of acid fog and corrosion.<sup>[2a,3]</sup> To accelerate the sluggish kinetics resulting from the extra water-dissociation step in alkaline electrolyte and to minimize the dynamic overpotential of the hydrogen evolution reaction (HER), efficient and highly stable catalysts, especially those that can sustain large current

L. B. Wu, F. H. Zhang, S. W. Song, M. H. Ning, L. Yu, S. Chen, Z. F. Ren  
Department of Physics and Texas Center for Superconductivity at the  
University of Houston (TcSUH)  
University of Houston  
Houston, TX 77204, USA  
E-mail: luoyu@mails.cnu.edu.cn; schen34@uh.edu; zren@uh.edu

L. B. Wu  
Materials Science and Engineering Program  
University of Houston  
Houston, TX 77204, USA

F. H. Zhang  
Department of Chemistry  
University of Houston  
Houston, TX 77204, USA

Q. Zhu  
Department of Mechanical Engineering  
Rice University  
Houston, TX 77005, USA

J. Q. Zhou  
Institute for Advanced Materials  
Hubei Normal University  
Huangshi 435002, China

G. H. Gao  
Department of Materials Science and Nano-Engineering  
Rice University  
Houston, TX 77005, USA

Z. Y. Chen, X. X. Xing, T. Tong, Y. Yao, J. M. Bao  
Department of Electrical and Computer Engineering and Texas Center  
for Superconductivity at the University of Houston (TcSUH)  
University of Houston  
Houston, TX 77204, USA

Q. C. Zhou  
College of Physical Science and Technology  
Central China Normal University  
Wuhan 430079, China

 The ORCID identification number(s) for the author(s) of this article can be found under <https://doi.org/10.1002/adma.202201774>.

DOI: 10.1002/adma.202201774

densities ( $\geq 500 \text{ mA cm}^{-2}$ ), are desirable.<sup>[4]</sup> To date, platinum (Pt)-based catalysts remain the benchmark HER catalysts in both acid and alkaline electrolytes. Unfortunately, the high costs and scarce sources for their constituent elements seriously limit the widespread utilization of these catalysts.<sup>[5]</sup> On the other hand, seawater electrolysis has recently attracted growing research interest due to the inexhaustible resource reserves and the great promise of massive hydrogen production without exacerbating freshwater shortages.<sup>[3b,6]</sup> However, the complicated composition of natural seawater can result in additional challenges for direct seawater electrolysis.<sup>[7]</sup> For example, the chlorine evolution reaction (CLER) from chloride ions ( $\text{Cl}^-$ ,  $\approx 0.5 \text{ M}$ ) in the seawater might compete with the oxygen evolution reaction (OER) on the anode and thus lower the overall seawater-electrolysis efficiency.<sup>[6a,b,8]</sup> Catalyst corrosion by chloride ions and poisoning by insoluble precipitates (dust, colloids, and bacteria) will degrade catalytic activity and durability.<sup>[3b,6b,9]</sup> Some recent works point out that corrosion-resistant electrolyzers and affordable membranes play important roles in direct seawater electrolysis, which can affect the device lifetime and efficiency of the system.<sup>[3b,10]</sup> All these challenges have greatly impeded the development of seawater-electrolysis technology.

Over the past decades, tremendous effort has been devoted to exploring efficient nonprecious catalysts intended to replace the Pt-based ones. Among these, transition metal nitrides (TMNs) have attracted considerable attention due to their high intrinsic catalytic activity, good electrical conductivity, and outstanding mechanical robustness.<sup>[11]</sup> Recent experimental and theoretical results suggest that TMNs have moderate binding capabilities toward reactants (water molecules, atomic hydrogen, or protons), allowing them outstanding HER catalytic activity.<sup>[11a,12]</sup> To further boost the alkaline HER performance of TMNs, effective sites for water dissociation should be introduced to enhance its sluggish kinetics. Thus, heterogeneous TMN-based catalysts, including  $\text{Ni}_3\text{N}/\text{Ni}$ ,  $\text{Co-Ni}_3\text{N}$ ,  $\text{V-Co}_4\text{N}$ ,  $\text{Cr-Co}_4\text{N}$ ,  $\text{Co/MoN}$ ,  $\text{Co-Mo}_5\text{N}_6$ , and  $\text{Ni}_{0.2}\text{Mo}_{0.8}\text{N}/\text{Ni}$ , in which either the introduced metallic atoms or the original metals in the TMNs serve as effective water-dissociation sites, have been synthesized and have shown comparable or even better HER performance than the benchmark Pt/C.<sup>[12c,13]</sup> However, studies of these heterogeneous TMN-based catalysts have mainly focused on freshwater electrolysis at small current densities usually lower than  $500 \text{ mA cm}^{-2}$ . For large-current-density water electrolysis, the catalytic performance might be limited by insufficient active sites and structural instability.<sup>[14]</sup> Additionally, scaling up alkaline water electrolysis technology and bringing it to market requires catalysts with practical catalytic performance under industrial conditions (normally in  $6 \text{ M KOH}$  at  $60\text{--}65^\circ\text{C}$ ) and affordable cost. Designing TMN-based catalysts with tailored structures, efficient catalytic activity, and long-term durability for large-current-density alkaline seawater electrolysis is very meaningful, although studies remain quite limited.<sup>[11g,15]</sup>

Here we demonstrate that a novel Ni-MoN catalyst consisting of dense crystalline Ni and MoN nanoparticles on an amorphous MoN nanorod matrix can be an efficient HER catalyst for both alkaline freshwater and seawater electrolysis. A nanorod-structured  $\text{NiMoO}_4 \cdot x\text{H}_2\text{O}$  precursor was first obtained through a scalable water bath reaction and was subsequently converted to a hierarchical nanorod-nanoparticle-structured

Ni-MoN catalyst with high surface roughness upon a second step of ammonia reduction. Its large surface area and multi-dimensional boundaries/defects can expose abundant active sites while its mesoporous structure (pore size of  $\approx 6.5 \text{ nm}$ ) and hydrophilic surface are beneficial for fast electrolyte diffusion and the quick release of gas bubbles. Theoretical calculations show that charge exchange and electron redistribution occur at the interfaces between Ni and MoN, so Ni-MoN is in a metallic state with high conductivity. The Mo sites in Ni-MoN have high capability toward water adsorption and dissociation, which greatly enhances the sluggish alkaline HER kinetics. Consequently, the optimized Ni-MoN catalyst achieves remarkable HER catalytic activity with ultralow overpotentials of 61 and 136 mV to drive large current densities of 100 and  $1000 \text{ mA cm}^{-2}$ , respectively, in  $1 \text{ M KOH}$  and exhibits a small Tafel slope of  $35.5 \text{ mV dec}^{-1}$ , placing it among the best self-supported HER catalysts reported thus far. It also has outstanding catalytic durability at constant current densities up to 100 and  $500 \text{ mA cm}^{-2}$  during 200 h of continuous testing. The Ni-MoN catalyst can well maintain its catalytic activity and durability in alkaline natural seawater and high-chlorine-concentration alkaline saline electrolytes. When coupled with a commercial stainless-steel mat (SSM), the Ni-MoN||SSM pair exhibits remarkable overall water/seawater electrolysis performance that is superior to the benchmark Pt/C||Ni-Fe layered double hydroxide (LDH) pair and many other catalysts, showing great potential for sustainable, efficient, and stable hydrogen production from water/seawater electrolysis.

## 2. Results and Discussion

As depicted in **Figure 1a**, a self-supported  $\text{NiMoO}_4 \cdot x\text{H}_2\text{O}$  precursor was first grown on copper foam (CF) through a water bath reaction at  $90^\circ\text{C}$  for 8 h, and it was subsequently converted to Ni-MoN through a second ammonia reduction step at  $400^\circ\text{C}$  for 2 h (see experimental details in the Supporting Information). Commercial CF was selected as a binder-free substrate for catalyst growth since it has the advantages of a 3D porous structure, high conductivity, and good chemical/mechanical stability. Photographs in **Figure S1a–c**, Supporting Information, show that the pristine CF substrate, the  $\text{NiMoO}_4 \cdot x\text{H}_2\text{O}$  precursor, and Ni-MoN are reddish, brown, and black, respectively, in color. Scanning electron microscopy (SEM, **Figure S2a–e**, Supporting Information) and transmission electron microscopy (TEM, **Figures S3a and S3d**, Supporting Information) characterizations indicate that  $\text{NiMoO}_4 \cdot x\text{H}_2\text{O}$  has a smooth 1D nanorod structure with diameters of between 100 and 200 nm. Such a nanorod-structured  $\text{NiMoO}_4 \cdot x\text{H}_2\text{O}$  precursor is different from the widely reported microrod- or microsheet-structured precursors produced through the hydrothermal reaction, and the smaller size of its constituent components will be beneficial for reacting with the ammonia flow during the subsequent ammonia reduction step.<sup>[13e,f,16]</sup> Corresponding energy dispersive spectroscopy (EDS) mapping images (**Figures S2f–h and S3e–g**, Supporting Information) and an EDS line scan curve (**Figure S3c**, Supporting Information) illustrate the uniform distribution of elemental Ni, Mo, and O throughout the skeleton of the CF substrate and inside each  $\text{NiMoO}_4 \cdot x\text{H}_2\text{O}$  nanorod.

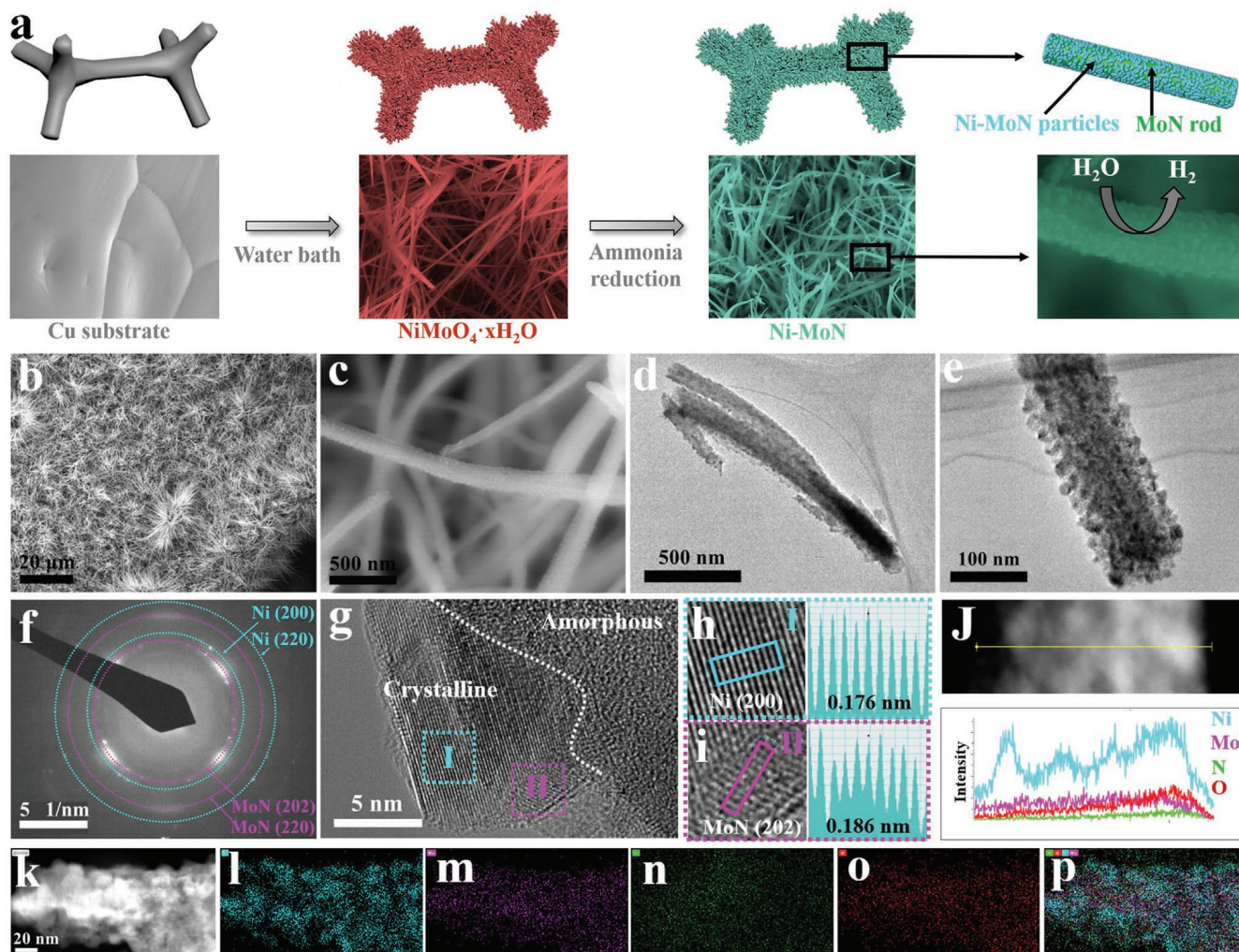


**Figure 1.** a) Schematic illustrations of the synthesis of Ni-MoN via a two-step water bath reaction-ammonia reduction procedure and corresponding SEM images at different synthesis stages. b,c) SEM images, d,e) TEM images, f) SAED pattern, and g-i) HRTEM images of Ni-MoN. j) EDS line scan and corresponding element dispersion of a single Ni-MoN nanorod. k) HAADF image of Ni-MoN and the corresponding EDS element mapping for l) Ni, m) Mo, n) N, o) O, and p) overlapped N, O, Ni, and Mo.

The X-ray diffraction (XRD) pattern in Figure S3h, Supporting Information, confirms the successful synthesis of the crystalline  $\text{NiMoO}_4 \cdot x\text{H}_2\text{O}$  phase. It should be noted that urea plays an important role in the synthesis process since  $\text{OH}^-$  from the urea can combine with metal cations to form metal hydroxides in the initial nucleation step and help to form nanorods during the water bath reaction.<sup>[17]</sup> The nanorod-structured precursor could not be obtained if urea were not added in the reactants, as shown in Figure S4, Supporting Information. After annealing in mixed ammonia–argon gas, the main structure of these vertical-standing nanorods was well preserved, and newly formed nanoparticles can be found on the surfaces of these nanorods (Figure 1b,c and Figure S5a–d, Supporting Information). Detailed TEM and aberration-corrected TEM (ACTEM) images in Figure 1d,e and Figure S6a,b, Supporting Information, show that these nanoparticles were embedded in the nanorod matrix and are several to tens of nanometers in diameter (inset, Figure S6a, Supporting Information). Such a hierarchical nanorod–nanoparticle structure with a high degree of surface

roughness not only exposes abundant active sites but also avoids catalyst aggregation during HER catalysis, benefiting the enhancement of both catalytic activity and durability.<sup>[18]</sup> Selected area electron diffraction (SAED), high-resolution TEM (HRTEM), and EDS characterizations were performed to identify the detailed compositions of the nanoparticles and nanorods. As shown in Figure 1f, characteristic (200) and (220) facets of metallic Ni and (202) and (220) facets of MoN can be distinguished within the SAED pattern, indicating a mixed composition of Ni and MoN in the hierarchical nanorod–nanoparticle-structured catalyst. The low-magnification HRTEM image in Figure S7a, Supporting Information, shows that the main part of the nanorod is in an amorphous state and the nanoparticles in the nanorod matrix are in a crystalline state. The interplanar spacings of the lattice fringes in the center of each crystalline nanoparticle were precisely measured to be 0.176 (Figure 1g,h and Figures S6b and S6d, Supporting Information) and 0.203 nm (Figure S6b,c, Supporting Information), corresponding to the (200) and (111) planes, respectively, of

metallic Ni. Additionally, a lattice fringe with an interplanar spacing of 0.186 nm, which is assigned to the (202) plane of MoN, can be found on the nanoparticle edges (Figure 1g,i). The phase boundaries between the amorphous nanorod matrix and the crystalline nanoparticles and between the metallic Ni and MoN phases, as well as the defects, can be clearly observed in the HRTEM image of Ni-MoN in Figure S7b, Supporting Information. These multidimensional boundaries and defects can expose more active sites for boosting the catalytic reaction.<sup>[19]</sup> The composition of Ni and MoN in the ammonia reduction product can further be confirmed by the EDS line scan curve in Figure 1j and the high-angle annular dark field (HAADF) EDS mapping images in Figure 1k–p and Figure S6e–j, Supporting Information, which show that elemental Ni gathers in the centers of the nanoparticles, while elemental Mo and N can both be found throughout the entire nanorod. Therefore, the nanorods in the hierarchical catalyst should mainly be composed of amorphous MoN, and the nanoparticles on the nanorods are mostly metallic Ni with a slight amount of MoN. It has been demonstrated that there might be a preferential reaction at the Ni sites in  $\text{NiMoO}_4 \cdot x\text{H}_2\text{O}$  and that Mo-oxide reduction may only proceed via gas spillover from the Ni sites when being annealed in a reductive gas flow.<sup>[20]</sup> Based on the characterizations above, the formation mechanism of Ni-MoN can be derived as follows: Ni sites are first reduced and gathered to form metallic Ni at the centers of the nanoparticles when being annealed in ammonia flow, and Mo combines with nitrogen in the excess ammonia gas to form crystalline MoN on the edges of, or amorphous MoN between, these Ni nanoparticles. Clearly, reductive ammonia gas, serving as both the reducing agent and the nitrogen source, is the key to generate this unique nanorod–nanoparticle structure, as proved by the smooth Ni–Mo–O product resulting from annealing the  $\text{NiMoO}_4 \cdot x\text{H}_2\text{O}$  precursor only in argon gas (Figure S8, Supporting Information). Additionally, the loss of  $\text{H}_2\text{O}$  molecules and elemental O due to the reaction with the flowing ammonia–argon gas, can create abundant atomic defects and lead to disordered atom packing in the nanorod matrix, forming amorphous regions. The uniformly dispersed nanorods effectively convert the CF substrate's hydrophobic surface (Figure S9a–c, Supporting Information) into a hydrophilic surface (Figures S9d–f and S9g–i, Supporting Information), which is beneficial for fast electrolyte diffusion, easy water molecule adsorption, and quick gas bubble release.<sup>[4b,12b]</sup>

The effects of water bath reaction time and the Ni:Mo ratio on the final morphology of Ni-MoN were investigated. Based on the SEM images of Ni-MoN catalysts produced with different water bath reaction time shown in Figure S10, Supporting Information, at least 6 h was required to obtain a homogenous nanorod structure. Here we used 8 h to ensure the complete and uniform growth of the  $\text{NiMoO}_4 \cdot x\text{H}_2\text{O}$  precursor. On the other hand, we found that the Ni:Mo ratio in the reactants did not have a significant effect on the nanorod structure but had a huge effect on the density of the Ni-MoN nanoparticles. Low Ni:Mo ratios of 2:7 (Figure S11a–c, Supporting Information) and 4:7 (Figure S11d–f, Supporting Information) resulted in sparse nanoparticles and a high Ni:Mo ratio of 12:7 (Figure S11g–i, Supporting Information) resulted in dense nanoparticles. This is because these nanoparticles are mainly composed of metallic

Ni and a higher Ni:Mo ratio is beneficial for forming denser Ni nanoparticles on the MoN matrix. For a comprehensive comparison, nickel nitride and molybdenum nitride catalysts were synthesized using a similar procedure except that no Mo or Ni source was added to the initial reactants for the respective catalysts. SEM images show that nickel nitride has a nanoparticle structure (Figure S12, Supporting Information) and molybdenum nitride has an irregular film structure (Figure S13, Supporting Information). Clearly, the combination of Ni and Mo is essential for obtaining a hierarchical nanorod–nanoparticle structure.

The phase composition and crystal structure of the hierarchical catalyst were further determined by XRD measurements. As shown in Figure 2a, the main peaks in the XRD pattern of Ni-MoN correspond to metallic nickel (Ni, JCPDS#04-0850) and molybdenum nitride (MoN, JCPDS#25-1367), which is consistent with the TEM results. The composition of the ammonia-treated catalysts can be tuned by varying the annealing temperature, as shown by the intensities of the diffraction peaks in the corresponding XRD patterns in Figure S14, Supporting Information. A low annealing temperature of 300 °C results in the catalyst being mainly composed of the  $\text{NiMoO}_4 \cdot x\text{H}_2\text{O}$  phase and a high temperature of 500 °C results in a mainly MoN-phase composition, which might be due to the weaker and stronger reactivity of ammonia species at low and high temperatures, respectively. When annealed at 700 °C, a new nitride phase of  $\text{Ni}_3\text{Mo}_3\text{N}$  appears and the metallic Ni phase disappears, which might be caused by the stronger reaction between Ni, Mo, and ammonia species. The XRD pattern of nickel nitride in Figure S15a, Supporting Information, shows peaks for both metallic nickel and nickel nitride ( $\text{Ni}_4\text{N}$ , JCPDS#36-1300), confirming a mixed composition of Ni and  $\text{Ni}_4\text{N}$ . There are no specific peaks in the XRD pattern of molybdenum nitride (Figure S15b, Supporting Information) due to its poor crystallinity, so we used Mo–N to represent its composition. The electron paramagnetic resonance (EPR) spectrum of Ni-MoN shows a stronger magnetic signal at  $\approx 3515$  G (g factor = 2.005) than that of the  $\text{NiMoO}_4 \cdot x\text{H}_2\text{O}$  precursor (Figure 2b), indicating a higher concentration of unpaired electrons resulting from structure defects.<sup>[21]</sup> The surface area of Ni-MoN was measured using the Brunauer–Emmett–Teller (BET) method and was found to be  $275 \text{ m}^2 \text{ g}^{-1}$  (Figure 2c), which is three times larger than that of the  $\text{NiMoO}_4 \cdot x\text{H}_2\text{O}$  precursor ( $76 \text{ m}^2 \text{ g}^{-1}$ ), indicating that the hierarchical nanorod–nanoparticle structure efficiently enlarges the surface area. Additionally, the nitrogen adsorption–desorption isotherm of Ni-MoN shows a typical IV hysteresis loop, suggesting that it has a mesoporous structure with an average pore size of  $\approx 6.5$  nm (inset, Figure 2c).<sup>[22]</sup> A large surface area can disperse abundant active sites and a mesoporous structure can provide additional pores for electrolyte diffusion, thereby promoting effective utilization of the catalyst during water electrolysis.

The surface chemical states of elemental Ni, Mo, and N for these catalysts were investigated by X-ray photoelectron spectroscopy (XPS). As shown in Figure 2d, two  $\text{Ni}^0$  peaks corresponding to metallic Ni can be observed at 853.4 and 870.6 eV for both Ni-MoN and Ni– $\text{Ni}_4\text{N}$  but are absent for  $\text{NiMoO}_4 \cdot x\text{H}_2\text{O}$ , which agrees well with the metallic Ni phase observed in the XRD patterns.<sup>[15]</sup> The remaining peaks in the

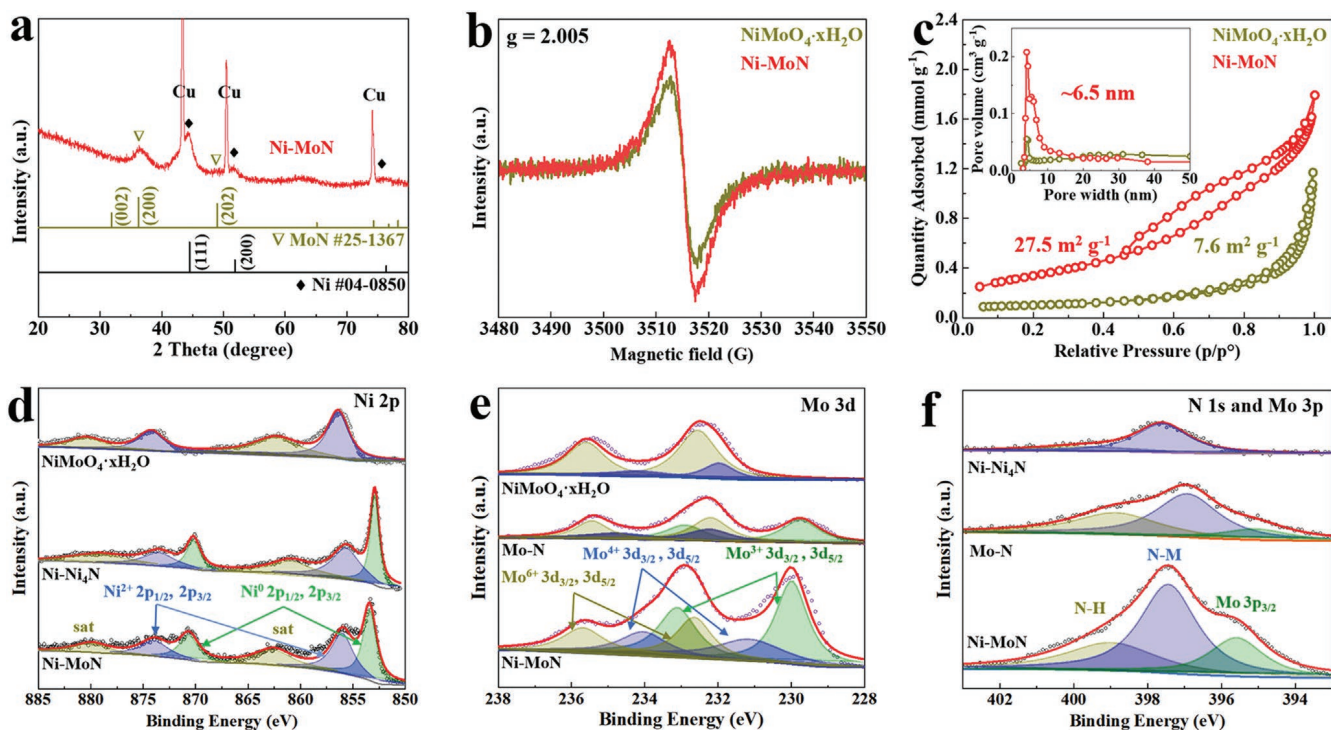


**Figure 2.** a) XRD pattern of Ni-MoN along with the standard PDF cards for Ni and MoN. b) EPR spectra and c) nitrogen adsorption–desorption isotherms and (inset) pore-size distribution curves of the  $\text{NiMoO}_4 \cdot x\text{H}_2\text{O}$  precursor and Ni-MoN. High-resolution XPS spectra of d) Ni, e) Mo, and f) N and Mo for the as-prepared catalysts.

XPS spectrum of Ni for Ni-MoN can be deconvoluted to  $\text{Ni}^{2+} 2p_{3/2}$  and  $\text{Ni}^{2+} 2p_{1/2}$  at 856.0 and 873.9 eV, respectively, along with a pair of satellite peaks, due to the inevitable surface oxidation of metallic Ni in the air.<sup>[3a,12c,13a,23]</sup> In the Mo XPS spectrum of Ni-MoN (Figure 2e), three doublets were observed: 230.0 and 233.1 ( $\text{Mo}^{3+} 3d_{5/2}$  and  $3d_{3/2}$ ), 231.3 and 234.2 ( $\text{Mo}^{4+} 3d_{5/2}$  and  $3d_{3/2}$ ), and 232.6 and 235.7 eV ( $\text{Mo}^{6+} 3d_{5/2}$  and  $3d_{3/2}$ ).<sup>[9a,13f]</sup> Compared with the Mo XPS spectrum of  $\text{NiMoO}_4 \cdot x\text{H}_2\text{O}$ , the presence of  $\text{Mo}^{3+}$  in that of Ni-MoN confirms the formation of MoN and the negative shift of  $\text{Mo}^{4+}$  indicates a lower valence state caused by the reduction of Mo species under the ammonia flow.<sup>[11b,24]</sup> The  $\text{Mo}^{3+}$  peaks in the Mo XPS spectrum of Ni-MoN show a positive shift compared to those for Mo–N, indicating a possible electron transfer from Mo to adjacent atoms.<sup>[13e]</sup> To reduce the interference of the surface oxidation and obtain accurate valence information regarding elemental Ni and Mo, we further applied XPS depth profiling to remove the surface of the Ni-MoN sample. As shown in Figure S16, Supporting Information, the XPS spectra for XPS-depth-profiled Ni-MoN have sharply reduced  $\text{Ni}^{2+}$  and  $\text{Mo}^{4+}$  peaks and an absence of  $\text{Mo}^{6+}$  peaks, indicating a deep reaction between the Ni and Mo cations and the reductive ammonia gas. Additionally, the peak intensities of  $\text{Ni}^0$  (metallic Ni) and  $\text{Mo}^{3+}$  (molybdenum nitride) are much stronger than those of  $\text{Ni}^{2+}$  (nickel oxide) and  $\text{Mo}^{4+}$  (molybdenum oxide), respectively, in the XPS spectra for XPS-depth-profiled Ni-MoN, confirming that elemental Ni and Mo in Ni-MoN mainly exist as metallic Ni and MoN rather than in oxide forms. Since the N 1s XPS spectrum of Ni-MoN is overlapped with that of Mo 3p (Figure 2f), three peaks were deconvoluted to Mo 3p at 395.6 eV, N–Mo or N–Ni at 397.5 eV, and

N–H at 399.0 eV.<sup>[9a]</sup> In the N 1s XPS spectrum for Ni– $\text{Ni}_4\text{N}$ , only a major peak attributed to N–Ni and a tiny peak attributed to N–H were found at 397.6 and 399.2 eV, respectively. Clearly, the N–Mo peak intensity in the XPS spectrum for Ni-MoN is much stronger than either the case of N–Ni in Ni– $\text{Ni}_4\text{N}$  or that of N–Mo in Mo–N, indicating a tight connection between Mo and N in Ni-MoN. Finally, there is no Cu signal in the Cu XPS spectra for either  $\text{NiMoO}_4 \cdot x\text{H}_2\text{O}$  or Ni-MoN (Figure S17, Supporting Information), indicating that the CF only served as a conductive substrate and did not leak into the catalysts.

The HER catalytic performance of the as-prepared catalysts was evaluated in a typical three-electrode configuration at a scan rate of  $1 \text{ mV s}^{-1}$ . For HER activity in alkaline water (1 M KOH), the linear sweep voltammetry (LSV) curves in Figure 3a show that our Ni-MoN requires very low overpotentials ( $\eta$ ) of 24 and 61 mV to attain current densities of 10 and  $100 \text{ mA cm}^{-2}$ , respectively, which is significantly smaller than those for the  $\text{NiMoO}_4 \cdot x\text{H}_2\text{O}$  precursor (269 and 423 mV), Ni– $\text{Ni}_4\text{N}$  (193 and 312 mV), and Mo–N (173 and 333 mV), as well as for the benchmark Pt/C (58 and 196 mV). The  $\eta_{100}$  of Ni-MoN (61 mV, where  $\eta_{100}$  is the overpotential required to attain a current density of  $100 \text{ mA cm}^{-2}$ ) is even lower than that of some recently reported self-supported noble-metal-based catalysts such as Pt– $\text{IrO}_2$  ( $\approx 70 \text{ mV}$ ),<sup>[25]</sup> Ru–MnFeP ( $\approx 73 \text{ mV}$ ),<sup>[26]</sup> Ru–CoP (74 mV),<sup>[27]</sup> Pt<sub>5A</sub>–NiO (85 mV),<sup>[28]</sup> and NiFeRu LDH ( $\approx 110 \text{ mV}$ ).<sup>[29]</sup> To achieve large current densities of 500 and  $1000 \text{ mA cm}^{-2}$ , which are required for commercial applications, the Ni-MoN catalyst only requires low overpotentials of 104 and 136 mV, respectively. Tafel slope values were calculated to reveal the intrinsic catalytic kinetics of the as-prepared catalysts. As

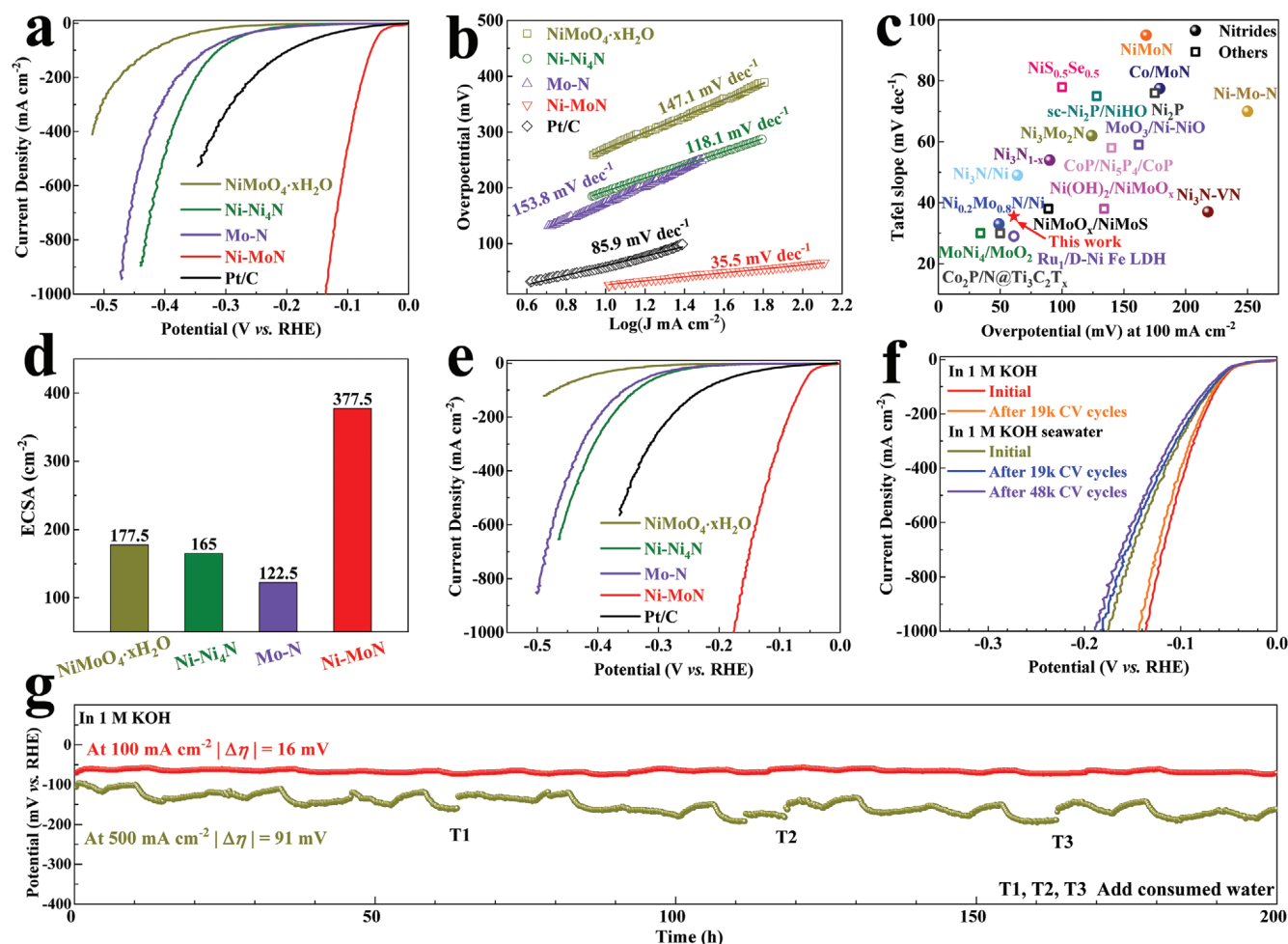


**Figure 3.** HER performance in 1 M KOH and 1 M KOH seawater electrolytes. a) LSV curves and b) corresponding Tafel plots of  $\text{NiMoO}_4 \cdot x\text{H}_2\text{O}$ ,  $\text{Ni-Ni}_4\text{N}$ ,  $\text{Mo-N}$ ,  $\text{Ni-MoN}$ , and  $\text{Pt/C}$  catalysts in 1 M KOH electrolyte. c) Comparison of HER catalytic activity in 1 M KOH electrolyte between  $\text{Ni-MoN}$  and recently reported self-supported nitride and other catalysts. d) ECSA values of  $\text{NiMoO}_4 \cdot x\text{H}_2\text{O}$ ,  $\text{Ni-Ni}_4\text{N}$ ,  $\text{Mo-N}$ , and  $\text{Ni-MoN}$ . e) LSV curves of the as-prepared catalysts in 1 M KOH seawater electrolyte. f) LSV curves of  $\text{Ni-MoN}$  before and after CV cycling in 1 M KOH and 1 M KOH seawater electrolytes. g) Chronopotentiometric curves of  $\text{Ni-MoN}$  at constant current densities of 100 and 500  $\text{mA cm}^{-2}$  in 1 M KOH electrolyte.

shown in Figure 3b,  $\text{Ni-MoN}$  has a small Tafel slope value of  $35.5 \text{ mV dec}^{-1}$ , which is less than one-quarter that of the  $\text{NiMoO}_4 \cdot x\text{H}_2\text{O}$  precursor ( $147.1 \text{ mV dec}^{-1}$ ), and is also much smaller than that of the comparison catalysts, including the benchmark  $\text{Pt/C}$ , indicating a higher transfer coefficient and enhanced catalytic kinetics.<sup>[17b,30]</sup> Such efficient HER catalytic activity places this  $\text{Ni-MoN}$  catalyst among the best documented self-supported nitride and other catalysts reported to date (Figure 3c and see Table S1, Supporting Information, for details). To determine the origin of the catalytic activity of  $\text{Ni-MoN}$ , electrochemical impedance spectroscopy (EIS), electrochemically active surface area (ECSA), and turnover frequency (TOF) analyses were performed. An amorphous phase normally exhibits structure disorder and loose atom packing, which is beneficial for fast ion diffusion and electron transfer.<sup>[31]</sup> Thus, the catalyst's amorphous nanorod structure not only serves as a matrix for dispersing catalytic-active  $\text{Ni-MoN}$  nanoparticles but also acts as an expressway for electron transfer. Based on the fitted Nyquist plots and the equivalent circuit shown in Figure S18, Supporting Information,  $\text{Ni-MoN}$  has

a much lower charge-transfer resistance ( $R_{ct}$ ) of  $\approx 2.7 \Omega$  at the electrode–electrolyte interface than that of the  $\text{NiMoO}_4 \cdot x\text{H}_2\text{O}$  precursor ( $\approx 161.6 \Omega$ ), suggesting a faster electron transport toward catalytic reaction. ECSA is usually calculated to evaluate the number of active sites, and it is proportional to the double-layer capacitance ( $C_{dl}$ ) shown in Figure S19, Supporting Information.<sup>[32]</sup> Benefiting from the hierarchical nanorod–nanoparticle structure, abundant phase boundaries, and high concentration of defects, the ECSA of  $\text{Ni-MoN}$  ( $377.5 \text{ cm}^2_{\text{ECSA}}$ ) is twice that of the  $\text{NiMoO}_4 \cdot x\text{H}_2\text{O}$  precursor ( $177.5 \text{ cm}^2_{\text{ECSA}}$ , Figure 3d), and much larger than that of the  $\text{Ni-Ni}_4\text{N}$  and  $\text{Mo-N}$  catalysts. When current density was normalized for ECSA (Figure S20, Supporting Information),  $\text{Ni-MoN}$  still exhibits the best HER performance among all the catalysts studied, confirming that it exhibits the highest intrinsic catalytic activity. Furthermore, TOF represents the number of molecules reacting per active site per unit of time and can be used to measure the instantaneous efficiency of a catalyst.<sup>[33]</sup> The TOF value for the  $\text{Ni-MoN}$  catalyst at the potential of  $-0.1 \text{ V}$  versus RHE is  $1.79 \text{ s}^{-1}$  (Figure S21, Supporting Information), which is much higher than that of

the  $\text{NiMoO}_4 \cdot x\text{H}_2\text{O}$  precursor ( $0.013 \text{ s}^{-1}$ ), indicating a high instantaneous efficiency for HER catalysis. Notably, all results from the EIS, ECSA, and TOF analyses agree well with the low overpotentials and small Tafel slope value of Ni-MoN shown in Figures 3a and 3b, respectively, suggesting its ultrahigh intrinsic HER activity.

To determine the best conditions for synthesizing the Ni-MoN catalyst, the influences of Ni:Mo ratio, ammonia-reduction temperature, and gas composition on its HER activity were investigated in detail. As shown in Figure S22, Supporting Information, all the Ni-MoN catalysts with different Ni:Mo ratios exhibit very good HER activity, and the one with a ratio of 8:7 shows the highest activity. As shown in Figure S14, Supporting Information, the ammonia-reduction temperature affects the phase composition, so it has a significant effect on the catalytic performance as well. A low temperature of  $300 \text{ }^\circ\text{C}$  and a high temperature of  $500 \text{ }^\circ\text{C}$  both lead to inferior HER activity (Figure S23, Supporting Information). The gas composition also greatly influences the catalytic activity. When annealed under argon flow only, the resultant Ni-Mo-O catalyst exhibits much worse HER activity than that of the Ni-MoN catalyst annealed in a mixed ammonia-argon flow, as shown in Figure S24, Supporting Information. The synthetic route used to prepare a catalyst determines its structure, and structure determines activity. Thus, the unique nanorod-nanoparticle-structured Ni-MoN produced using a novel synthesis method can enable enhanced catalytic performance. Compared with Ni-MoN catalysts that have a microrod-nanoparticle (Figure S25, Supporting Information) or microsheet-nanoparticle (Figure S26, Supporting Information) structure synthesized via a hydrothermal reaction-ammonia reduction procedure, nanorod-nanoparticle-structured Ni-MoN has a denser nanorod matrix for dispersing catalytic-active Ni-MoN nanoparticles. The smaller size can help to promote the mass transfer process. As a result, the nanorod-nanoparticle-structured Ni-MoN catalyst has higher apparent and intrinsic HER catalytic activity compared with the microstructured Ni-MoN catalysts (Figure S27, Supporting Information).

Seawater electrolysis is attracting increasing research interest due to the inexhaustible reserves of feedstock.<sup>[3b,6a]</sup> Considering the remarkable HER performance of Ni-MoN in alkaline water, we then measured its hydrogen-generation ability in alkaline natural seawater (1 M KOH seawater). As shown in Figure 3e, compared with their corresponding LSV curves in 1 M KOH (Figure 3a), all five as-prepared catalysts show a decline in activity in 1 M KOH seawater, which could be caused by the obstruction of active sites and the degradation in conductivity in the complicated natural seawater electrolyte. However, our Ni-MoN catalyst still exhibits very good HER activity with limited degradation in 1 M KOH seawater electrolyte. Specifically, it requires overpotentials of 29, 66, 128, and 176 mV to attain current densities of 10, 100, 500, and  $1000 \text{ mA cm}^{-2}$ , respectively, in 1 M KOH seawater. The corresponding Tafel slope of Ni-MoN in 1 M KOH seawater is  $36.8 \text{ mV dec}^{-1}$  (Figure S28a, Supporting Information), close to that in 1 M KOH, showing good retention of catalytic activity. Considering that the concentration of NaCl in seawater electrolyte will increase due to the continuous consumption of water during the process of seawater catalysis, we then measured the catalytic activity of Ni-MoN in a harsh

chlorine environment to verify its robustness against corrosive chlorine. As shown in Figure S29a, Supporting Information, the catalytic activity of Ni-MoN in 1 M KOH + 0.5 M NaCl (alkaline simulated seawater) is close to that in 1 M KOH electrolyte. After further increasing the chlorine concentration (1 M KOH + 1 M NaCl and 1 M KOH + 2 M NaCl), the HER activity exhibits slight decay, but is still better than the performance in alkaline natural seawater, demonstrating good chlorine-resistant performance.

For practical application of a catalyst, its durability must be taken into consideration. To verify the durability of the Ni-MoN catalyst, HER LSV curves were recorded before and after CV cycling in both 1 M KOH and 1 M KOH seawater electrolytes. As shown in Figure 3f, after 19 000 (19k) CV cycles in 1 M KOH electrolyte, the resultant LSV curve (orange) shows a slight decline compared with the initial curve (red). Even after 48k CV cycles in 1 M KOH seawater electrolyte (violet), the required overpotential of the Ni-MoN catalyst only increased by 1, 5, 10, and 13 mV to attain current densities of 10, 100, 500, and  $1000 \text{ mA cm}^{-2}$ , respectively, compared with its initial catalytic performance in 1 M KOH seawater electrolyte (brown). Figure 3g shows the results of long-term stability tests of the Ni-MoN catalyst performed at constant current densities. It can be seen that the potential fluctuation at a current density of  $100 \text{ mA cm}^{-2}$  over 200 h continuous testing in 1 M KOH is only 16 mV, which is superior to that of all the self-supported catalysts listed in Table S1, Supporting Information. The hierarchical nanorod-nanoparticle structure and large surface area of Ni-MoN can provide abundant active sites for water electrolysis and its hydrophilic surface helps to achieve accelerated gas-release capabilities. As a result, the hydrogen gas bubbles, when still very small in size, can be released rapidly from numerous active sites as shown in Figure S30a and Video S1, Supporting Information. A previous study confirms that a hydrophilic surface normally possesses very low adhesive force between the gas bubbles and the catalyst, which might be good for catalytic stability.<sup>[18a]</sup> On the other hand, the hydrogen gas bubbles will remain attached to the hydrophobic surface of CF and merge together into large-size bubbles as shown in Figure S30b and Video S2, Supporting Information. These large-size bubbles will prevent the further contact between the active sites and the electrolyte and their bursting can cause resistance/potential fluctuations.<sup>[34]</sup> Furthermore, the Ni-MoN catalyst can work well at the industry-standard current density of  $500 \text{ mA cm}^{-2}$  for over 200 h, showing a great potential for practical application. Even in 1 M KOH seawater electrolyte (Figure S28b, Supporting Information), this catalyst can work stably over 100 h at a large current density of  $500 \text{ mA cm}^{-2}$  with an affordable overpotential fluctuation of 47 mV. When measured at a constant current density of  $100 \text{ mA cm}^{-2}$  in harsh chlorine electrolytes, the Ni-MoN catalyst operated well for 115 h and did not show much increase in overpotential (23 mV in total, Figure S29b, Supporting Information). We further investigated changes in the morphology and composition of the Ni-MoN catalyst after long-term stability testing for HER catalysis. SEM images (Figures S31a–d and S32a–e, Supporting Information) show that the 3D hierarchical structure of Ni-MoN was maintained except that some of the catalyst was peeled off after long-term operation of over 8 days in 1 M KOH or nearly

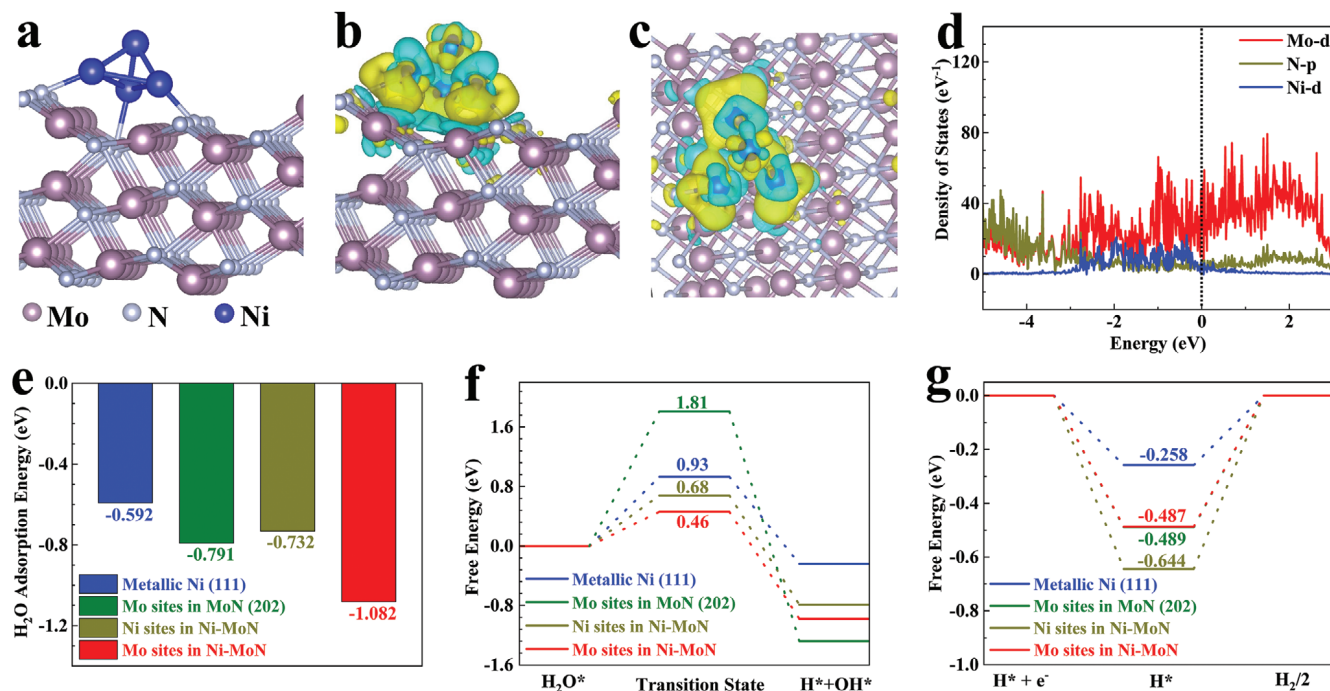


**Figure 4.** a) Ni-MoN model for DFT calculations. b) Side and c) top views of charge density differences in Ni-MoN. Yellow and cyan regions represent electron accumulation and depletion, respectively. d) DOS calculated for Mo, N, and Ni in Ni-MoN. The black dotted line indicates the Fermi level. e) Adsorption energy of H<sub>2</sub>O, f) energy diagram for H<sub>2</sub>O dissociation, and g) free energy diagram for H adsorption for metallic Ni, Mo sites in MoN, and Ni and Mo sites in Ni-MoN.

5 days in alkaline saline electrolytes. TEM (Figure S31e–g, Supporting Information), XPS (Figure S31h, Supporting Information), Raman (Figure S31i, Supporting Information), and EDS (Figure S32g, Supporting Information) results together reveal that some nanosheets formed on the surfaces of the nanorods after HER stability testing, and their composition was identified as a mixture of NiOOH and NiO, which is consistent with previous reports.<sup>[13f,35]</sup>

To gain molecular-level insights into the high catalytic activity of Ni-MoN, density functional theory (DFT) calculations were performed. A typical Ni-MoN model consisting of metallic Ni clusters on MoN (202) was built and is shown in Figure 4a and Figure S33a,b, Supporting Information. The charge density differences (Figure 4b,c) illustrate that there is electron accumulation at the heterointerface, suggesting a strong charge exchange and electronic tuning between Ni and MoN.<sup>[36]</sup> The electronic structure tuning in Ni-MoN can also be confirmed by the charge density distributions displayed in Figure S34, Supporting Information, which shows that there is an accumulation of charge density on both the N and Mo sites, unlike the case of MoN.<sup>[37]</sup> The successive distribution of the density of states (DOS) near the Fermi level, as shown in Figure 4d, indicates that Ni-MoN is in a metallic state, which is beneficial for achieving high electronic conductivity.<sup>[12b,24]</sup> The Tafel slope value of Ni-MoN is 35.5 mV dec<sup>-1</sup>, suggesting that the catalytic pathway of Ni-MoN follows a Volmer (H<sub>2</sub>O dissociation, M + H<sub>2</sub>O + e<sup>-</sup> → M–H\* + OH<sup>-</sup>)-Heyrovsky (H adsorption/desorption, M–H\* + H<sub>2</sub>O + e<sup>-</sup> → M + OH<sup>-</sup> + H<sub>2</sub>) routine.<sup>[4a,12b,19b,38]</sup> Therefore, we further calculated the H<sub>2</sub>O adsorption energy, the energy barrier of H<sub>2</sub>O dissociation, and the H adsorption/desorption energy to deeply understand

the Volmer–Heyrovsky pathway for the Ni-MoN catalyst. The models for DFT calculations include the (111) facet of metallic Ni, the (202) facet of pristine MoN, Ni sites on top of the Ni clusters in Ni-MoN, and Mo sites near the interface between Ni and MoN in Ni-MoN, and corresponding reaction pathways are shown in Figures S35–S38, Supporting Information. Figure 4e shows that the Mo sites in Ni-MoN possess much lower adsorption energy for H<sub>2</sub>O molecules (–1.082 eV) than the other three sites, indicating more favorable H<sub>2</sub>O adsorption on the surface of Mo sites in Ni-MoN.<sup>[3a]</sup> This is important for boosting alkaline HER since absorption of H<sub>2</sub>O molecules is the preliminary step for the subsequent H<sub>2</sub>O dissociation process.<sup>[12b]</sup> Figure 4f shows the H<sub>2</sub>O dissociation energy results, from which it can be seen that the energy barrier of water dissociation (ΔG<sub>H<sub>2</sub>O</sub>) on metallic Ni and Mo sites in MoN are as high as 0.93 and 1.81 eV, respectively. In contrast, the ΔG<sub>H<sub>2</sub>O</sub> on Ni-MoN, especially on the Mo sites in Ni-MoN, is significantly decreased to 0.46 eV, suggesting accelerated H<sub>2</sub>O dissociation kinetics.<sup>[25]</sup> This is crucial for alkaline HER catalysis, in which the Volmer step (H<sub>2</sub>O dissociation) has been regarded as the rate-determining step (RDS).<sup>[39]</sup> The hydrogen adsorption energy (ΔG<sub>H\*</sub>) on the Mo sites in Ni-MoN was calculated to be –0.487 eV (Figure 4g), the absolute value of which is smaller than that on Ni sites in Ni-MoN (–0.644 eV), from which it can be inferred that Mo sites are more favorable for H adsorption and desorption during the Heyrovsky step.<sup>[24,38]</sup> It should be noted that although metallic Ni shows the lowest absolute value of ΔG<sub>H\*</sub> (–0.258 eV), its sluggish H<sub>2</sub>O dissociation and inferior H<sub>2</sub>O absorption ability restrict its catalytic performance. To eliminate the influence of structural difference between metallic Ni and Ni cluster on the theoretical calculation results, we constructed a pristine

Ni cluster model (Figure S33g,h, Supporting Information) for DFT calculations and a corresponding reaction pathway, and DFT calculation results are shown in Figures S39 and S40, Supporting Information, respectively. Clearly, the combination of Ni and MoN lead to higher  $\Delta G_{\text{H}_2\text{O}}$  on Ni sites and lower  $\Delta G_{\text{H}_2\text{O}}$  on Mo sites in Ni-MoN compared with that on the pristine Ni cluster and the pristine MoN phase. Therefore, the DFT calculation results demonstrate that the introduction of Ni effectively regulates the electronic structure of MoN, which endows Mo sites in Ni-MoN with a high capability towards  $\text{H}_2\text{O}$  adsorption and dissociation, thus contributing to the catalyst's outstanding HER activity in alkaline media.

We then coupled our Ni-MoN catalyst with commercial stainless-steel mat (SSM) in an H-type electrolyzer with an anion exchange membrane (AEM) in the middle for overall water/seawater electrolysis. The silver-colored SSM electrode (Figure S1d, Supporting Information) has a dense microrod structure (Figure S41a–e, Supporting Information) with a mixed com-

position of Fe, Cr, Ni, and Mo (Figure S41f–i, Supporting Information).<sup>[40]</sup> For comparison, we grew Ni-Fe LDH, one of the most OER-active catalysts, on CF (Figure S42, Supporting Information) using a similar water bath reaction method as for Ni-MoN and then paired it with the benchmark HER catalyst Pt/C for overall water/seawater electrolysis. Impressively, the Ni-MoN||SSM pair outperforms the benchmark Pt/C||Ni-Fe LDH pair as shown in Figure 5a. This good electrolyzer requires voltages of only 1.613 (1.635) and 1.711 (1.783) V to attain current densities of 100 and 500  $\text{mA cm}^{-2}$  in 1 M KOH (1 M KOH seawater) electrolyte, respectively (Figure 5b), which are significantly lower than those for the Pt/C||Ni-Fe LDH pair. Such low voltage requirements to drive a current density of 100  $\text{mA cm}^{-2}$  make this electrolyzer outperform many recently reported catalysts (Figure 5c and see Table S2, Supporting Information, for details) for overall water/seawater electrolysis. For an even larger current density of 1000  $\text{mA cm}^{-2}$ , the Ni-MoN||SSM pair requires voltages of 1.779 and 1.885 V in 1 M KOH and 1 M

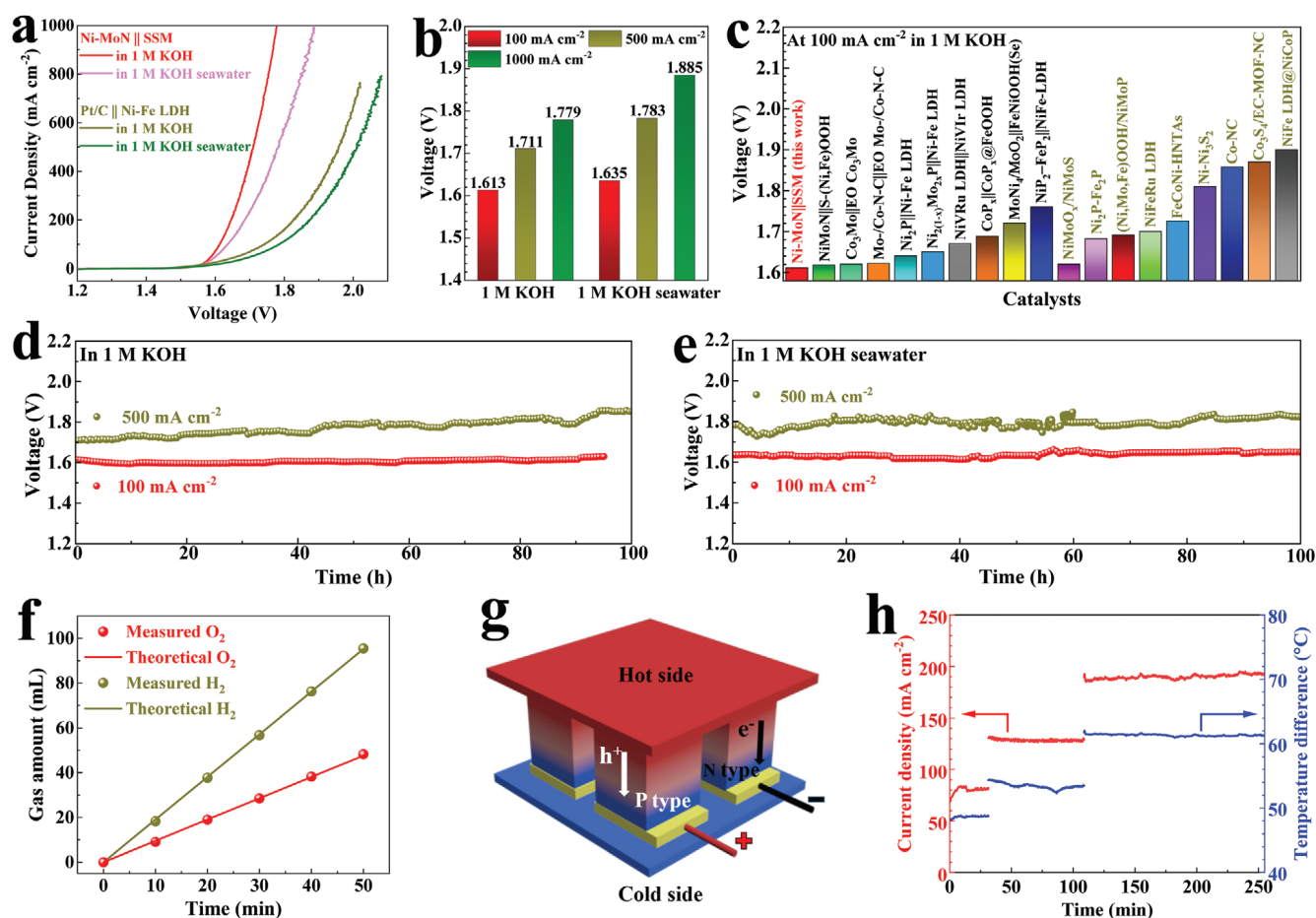


**Figure 5.** a) Overall water/seawater electrolysis performance of Ni-MoN||SSM and Pt/C||Ni-Fe LDH pairs in 1 M KOH and 1 M KOH seawater electrolytes. b) Voltages required for the Ni-MoN||SSM pair to achieve current densities of 100, 500, and 1000  $\text{mA cm}^{-2}$  in 1 M KOH and 1 M KOH seawater electrolytes. c) Comparison of the voltages required to achieve a current density of 100  $\text{mA cm}^{-2}$  for overall water electrolysis between the Ni-MoN||SSM pair and other self-supported catalysts in 1 M KOH electrolyte. Brown labels: bifunctional catalysts. Chronopotentiometric curves of the Ni-MoN||SSM pair at constant current densities of 100 and 500  $\text{mA cm}^{-2}$  for overall water/seawater electrolysis in d) 1 M KOH and e) 1 M KOH seawater electrolytes at room temperature. f) Measured (dots) and theoretical (solid lines) gaseous products from the Ni-MoN||SSM pair at a current density of 500  $\text{mA cm}^{-2}$  in 1 M KOH seawater electrolyte. g) Schematic illustration of the principle for power generation by a TE device. h) Real-time dynamics of current density attained by the Ni-MoN||SSM electrolyzer in 1 M KOH driven by a TE device (red) and real-time temperature gradient between the hot and cold sides of the TE device (blue).

KOH seawater electrolytes, respectively, demonstrating remarkable catalytic activity. We also measured the catalytic activity of Ni-MoN and the Ni-MoN||SSM pair under industrial conditions (in 6 M KOH electrolyte at 60 °C), and the results are shown in Figure S43a,b, Supporting Information. In particular, to achieve an ultrahigh current density of 3000 mA cm<sup>-2</sup> in 6 M KOH and 6 M KOH seawater electrolytes at 60 °C for HER, the Ni-MoN catalyst requires low overpotentials of 152 and 244 mV, respectively. For overall water and seawater electrolysis under these conditions, the Ni-MoN||SSM pair requires voltages of only 1.690 and 1.718 V, respectively, to reach the ultrahigh current density of 3000 mA cm<sup>-2</sup>. Long-term stability of the Ni-MoN||SSM pair was assessed at constant current densities and the results are shown in Figure 5d,e. At a constant current density of 100 mA cm<sup>-2</sup> at room temperature, this electrolyzer can work effectively for ≈100 h in both 1 M KOH and 1 M KOH seawater electrolytes with only slight fluctuations of 36 and 48 mV, respectively. In addition, when measured in 6 M KOH electrolyte at 60 °C, this Ni-MoN||SSM pair can work efficiently at 500 mA cm<sup>-2</sup> for more than 110 h (Figure S43c, Supporting Information), indicating a great potential for realistic industrial freshwater electrolysis. Although there was some voltage fluctuation under a large current density of 500 mA cm<sup>-2</sup> in 1 M KOH seawater at room temperature, the Ni-MoN||SSM pair still operated well for 100 h, indicating good stability for hydrogen production via seawater electrolysis. A major concern for large-current-density seawater electrolysis is competition from the chlorine evolution reaction (ClER) on the anode, so we investigated the possible formation of hypochlorite in the electrolyte using a colorimetric reagent after overall seawater electrolysis at 500 mA cm<sup>-2</sup> for 100 h. As shown in Figure S44, Supporting Information, there was no color change in the reagent, indicating that no hypochlorite was formed during seawater electrolysis at such a large current density. Faradaic efficiency (FE) of the Ni-MoN||SSM pair for overall seawater electrolysis was measured at a constant current density of 500 mA cm<sup>-2</sup> using the drainage method shown in Figure S45, Supporting Information. The resultant data was collected and is displayed in Figure 5f, which shows that the produced H<sub>2</sub> and O<sub>2</sub> gas amounts match well with the theoretical values, indicating the high FE of this electrolyzer. Finally, we used a commercial thermoelectric (TE) module, a device that can convert thermal energy into electricity (Figure 5g), to drive the Ni-MoN||SSM pair in 1 M KOH electrolyte. Encouragingly, our electrolyzer can be effectively driven by a single TE module on a homemade testing platform with temperature differences of ≈49, ≈54, and ≈61 °C for output current densities of 83, 129, and 190 mA cm<sup>-2</sup>, respectively, as shown in Figure 5h. The corresponding Video S3, Supporting Information, recorded during testing at the temperature difference of 61 °C shows that abundant hydrogen bubbles were generated on, and immediately released from, the surface of the Ni-MoN catalyst, demonstrating that waste heat can be efficiently converted into valuable hydrogen energy through water electrolysis.

### 3. Conclusion

A heterogeneous Ni-MoN catalyst consisting of metallic Ni and MoN was synthesized and exhibits outstanding HER per-

formance in both alkaline water and seawater electrolytes. Structure characterizations show that it has a hierarchical nanorod–nanoparticle structure with a large surface area, multi-dimensional boundaries/defects, and a hydrophilic surface. These characteristics allow Ni-MoN to possess abundant active sites and accelerated gas-release capabilities and to effectively avoid catalyst degradation during HER catalysis, especially at large current densities. Experimental results and DFT calculations together prove that the combination of metallic Ni and MoN can modulate the electron redistribution and enhance the sluggish water-dissociation kinetics. As a result, this Ni-MoN catalyst demonstrates remarkable HER catalytic activity and durability, outperforming the benchmark Pt/C and many other efficient alkaline HER catalysts. When Ni-MoN is coupled with SSM, an OER catalyst, the Ni-MoN||SSM pair is outstanding in overall water/seawater electrolysis, showing great promise for large-scale H<sub>2</sub> production.

### Supporting Information

Supporting Information is available from the Wiley Online Library or from the author.

### Acknowledgements

L.B.W. and F.H.Z. contributed equally to this work. The authors thank Prof. Boris Makarenko in the Department of Chemistry at University of Houston for assistance in conducting XPS depth profiling analysis. The authors thank Prof. Yimo Han in the Electron Microscopy Center at Rice University for assistance in conducting ACTEM measurement. Element Resources, LLC funded part of the work.

### Conflict of Interest

The authors declare no conflict of interest.

### Data Availability Statement

The data that support the findings of this study are available from the corresponding author upon reasonable request.

### Keywords

hierarchical structures, hydrogen evolution reaction, Ni-MoN catalysts, seawater electrolysis, water dissociation

Received: February 23, 2022

Revised: March 20, 2022

Published online: April 24, 2022

- [1] a) C. G. Morales-Guio, L. A. Stern, X. Hu, *Chem. Soc. Rev.* **2014**, *43*, 6555; b) X. Zou, Y. Zhang, *Chem. Soc. Rev.* **2015**, *44*, 5148; c) Z. W. Seh, J. Kibsgaard, C. F. Dickens, I. Chorkendorff, J. K. Nørskov, T. F. Jaramillo, *Science* **2017**, *355*, eaad4998; d) L. An, C. Wei, M. Lu, H. Liu, Y. Chen, G. G. Scherer, A. C. Fisher, P. Xi, Z. J. Xu, C. H. Yan, *Adv. Mater.* **2021**, *33*, 2006328.

- [2] a) J. Wang, F. Xu, H. Jin, Y. Chen, Y. Wang, *Adv. Mater.* **2017**, *29*, 1605838; b) D. Y. Li, L. L. Liao, H. Q. Zhou, Y. Zhao, F. M. Cai, J. S. Zeng, F. Liu, H. Wu, D. S. Tang, F. Yu, *Mater. Today Phys.* **2021**, *16*, 100314.
- [3] a) L. Yu, I. K. Mishra, Y. Xie, H. Zhou, J. Sun, J. Zhou, Y. Ni, D. Luo, F. Yu, Y. Yu, S. Chen, Z. Ren, *Nano Energy* **2018**, *53*, 492; b) W. Tong, M. Forster, F. Dionigi, S. Dresp, R. Sadeghi Erami, P. Strasser, A. J. Cowan, P. Farràs, *Nat. Energy* **2020**, *5*, 367.
- [4] a) X. Wu, S. Zhou, Z. Wang, J. Liu, W. Pei, P. Yang, J. Zhao, J. Qiu, *Adv. Energy Mater.* **2019**, *9*, 1901333; b) Y. Luo, L. Tang, U. Khan, Q. Yu, H. M. Cheng, X. Zou, B. Liu, *Nat. Commun.* **2019**, *10*, 269; c) S. Dresp, T. Ngo Thanh, M. Klingenhof, S. Brückner, P. Hauke, P. Strasser, *Energy Environ. Sci.* **2020**, *13*, 1725.
- [5] a) Z. Wang, J. Fan, B. Cheng, J. Yu, J. Xu, *Mater. Today Phys.* **2020**, *15*, 100279; b) L. Yang, Z. Liu, S. Zhu, L. Feng, W. Xing, *Mater. Today Phys.* **2021**, *16*, 100292.
- [6] a) S. Dresp, F. Dionigi, M. Klingenhof, P. Strasser, *ACS Energy Lett.* **2019**, *4*, 933; b) Y. Kuang, M. J. Kenney, Y. Meng, W.-H. Hung, Y. Liu, J. E. Huang, R. Prasanna, P. Li, Y. Li, L. Wang, M.-C. Lin, M. D. McGehee, X. Sun, H. Dai, *Proc. Natl. Acad. Sci. U. S. A.* **2019**, *116*, 6624; c) F. Zhang, L. Yu, L. Wu, D. Luo, Z. Ren, *Trends Chem.* **2021**, *3*, 485; d) L. Wu, L. Yu, B. McElhenny, X. Xing, D. Luo, F. Zhang, J. Bao, S. Chen, Z. Ren, *Appl. Catal. B* **2021**, *294*, 120256.
- [7] a) J. E. Bennett, *Int. J. Hydrogen Energy* **1980**, *5*, 401; b) F. J. Millero, R. Feistel, D. G. Wright, T. J. McDougall, *Deep Sea Res., Part I* **2008**, *55*, 50; c) F. Dionigi, T. Reier, Z. Pawolek, M. Gliech, P. Strasser, *ChemSusChem* **2016**, *9*, 962.
- [8] M. Ning, L. Wu, F. Zhang, D. Wang, S. Song, T. Tong, J. Bao, S. Chen, L. Yu, Z. Ren, *Mater. Today Phys.* **2021**, *19*, 100419.
- [9] a) L. Yu, Q. Zhu, S. Song, B. McElhenny, D. Wang, C. Wu, Z. Qin, J. Bao, Y. Yu, S. Chen, Z. Ren, *Nat. Commun.* **2019**, *10*, 5106; b) L. Yu, L. Wu, B. McElhenny, S. Song, D. Luo, F. Zhang, Y. Yu, S. Chen, Z. Ren, *Energy Environ. Sci.* **2020**, *13*, 3439; c) J. Chang, G. Wang, Z. Yang, B. Li, Q. Wang, R. Kuliiev, N. Orlovskaya, M. Gu, Y. Du, G. Wang, Y. Yang, *Adv. Mater.* **2021**, *33*, 2101425.
- [10] a) S. Dresp, F. Dionigi, S. Loos, J. Ferreira de Araujo, C. Spöri, M. Gliech, H. Dau, P. Strasser, *Adv. Energy Mater.* **2018**, *8*, 1800338; b) Y. S. Park, J. Lee, M. J. Jang, J. Yang, J. Jeong, J. Park, Y. Kim, M. H. Seo, Z. Chen, S. M. Choi, *J. Mater. Chem. A* **2021**, *9*, 9586.
- [11] a) H. Wang, J. Li, K. Li, Y. Lin, J. Chen, L. Gao, V. Nicolosi, X. Xiao, J. M. Lee, *Chem. Soc. Rev.* **2021**, *50*, 1354; b) Y. Zhang, B. Ouyang, J. Xu, S. Chen, R. S. Rawat, H. J. Fan, *Adv. Energy Mater.* **2016**, *6*, 1600221; c) H. Yan, Y. Xie, A. Wu, Z. Cai, L. Wang, C. Tian, X. Zhang, H. Fu, *Adv. Mater.* **2019**, *31*, 1901174; d) Y. Li, X. Wei, L. Chen, J. Shi, M. He, *Nat. Commun.* **2019**, *10*, 5335; e) X. H. Chen, Q. Zhang, L. L. Wu, L. Shen, H. C. Fu, J. Luo, X. L. Li, J. L. Lei, H. Q. Luo, N. B. Li, *Mater. Today Phys.* **2020**, *15*, 100268; f) Y. Hu, T. Xiong, M. S. J. T. Balogun, Y. Huang, D. Adekoya, S. Zhang, Y. Tong, *Mater. Today Phys.* **2020**, *15*, 100267; g) H. Jin, X. Liu, A. Vasileff, Y. Jiao, Y. Zhao, Y. Zheng, S. Z. Qiao, *ACS Nano* **2018**, *12*, 12761; h) H. Jin, T. Song, U. Paik, S.-Z. Qiao, *Acc. Mater. Res.* **2021**, *2*, 559.
- [12] a) B. Cao, G. M. Veith, J. C. Neufeind, R. R. Adzic, P. G. Khalifah, *J. Am. Chem. Soc.* **2013**, *135*, 19186; b) B. Liu, B. He, H. Q. Peng, Y. Zhao, J. Cheng, J. Xia, J. Shen, T. W. Ng, X. Meng, C. S. Lee, W. Zhang, *Adv. Sci.* **2018**, *5*, 1800406; c) F. Song, W. Li, J. Yang, G. Han, P. Liao, Y. Sun, *Nat. Commun.* **2018**, *9*, 4531.
- [13] a) C. Zhu, A. L. Wang, W. Xiao, D. Chao, X. Zhang, N. H. Tiep, S. Chen, J. Kang, X. Wang, J. Ding, J. Wang, H. Zhang, H. J. Fan, *Adv. Mater.* **2018**, *30*, 1705516; b) Z. Chen, Y. Song, J. Cai, X. Zheng, D. Han, Y. Wu, Y. Zang, S. Niu, Y. Liu, J. Zhu, X. Liu, G. Wang, *Angew. Chem., Int. Ed.* **2018**, *57*, 5076; c) N. Yao, P. Li, Z. Zhou, Y. Zhao, G. Cheng, S. Chen, W. Luo, *Adv. Energy Mater.* **2019**, *9*, 1902449; d) J. Sun, W. Xu, C. Lv, L. Zhang, M. Shakouri, Y. Peng, Q. Wang, X. Yang, D. Yuan, M. Huang, Y. Hu, D. Yang, L. Zhang, *Appl. Catal. B* **2021**, *286*, 119882; e) F. Lin, Z. Dong, Y. Yao, L. Yang, F. Fang, L. Jiao, *Adv. Energy Mater.* **2020**, *10*, 2002176; f) B. Zhang, L. Zhang, Q. Tan, J. Wang, J. Liu, H. Wan, L. Miao, J. Jiang, *Energy Environ. Sci.* **2020**, *13*, 3007.
- [14] H. Sun, Z. Yan, F. Liu, W. Xu, F. Cheng, J. Chen, *Adv. Mater.* **2020**, *32*, 1806326.
- [15] H. Jin, X. Wang, C. Tang, A. Vasileff, L. Li, A. Slattery, S. Z. Qiao, *Adv. Mater.* **2021**, *33*, 2007508.
- [16] a) S. Peng, L. Li, H. B. Wu, S. Madhavi, X. W. D. Lou, *Adv. Energy Mater.* **2015**, *5*, 1401172; b) J. Zhang, T. Wang, P. Liu, Z. Liao, S. Liu, X. Zhuang, M. Chen, E. Zschech, X. Feng, *Nat. Commun.* **2017**, *8*, 15437.
- [17] a) K. Yan, G. Wu, W. Jin, *Energy Technol.* **2016**, *4*, 354; b) L. Wu, L. Yu, X. Xiao, F. Zhang, S. Song, S. Chen, Z. Ren, *Research* **2020**, *2020*, 3976278.
- [18] a) H. Li, S. Chen, Y. Zhang, Q. Zhang, X. Jia, Q. Zhang, L. Gu, X. Sun, L. Song, X. Wang, *Nat. Commun.* **2018**, *9*, 2452; b) C. Liang, P. Zou, A. Nairan, Y. Zhang, J. Liu, K. Liu, S. Hu, F. Kang, H. J. Fan, C. Yang, *Energy Environ. Sci.* **2020**, *13*, 86.
- [19] a) H. Han, H. Choi, S. Mhin, Y.-R. Hong, K. M. Kim, J. Kwon, G. Ali, K. Y. Chung, M. Je, H. N. Umh, D.-H. Lim, K. Davey, S.-Z. Qiao, U. Paik, T. Song, *Energy Environ. Sci.* **2019**, *12*, 2443; b) S. Jiao, X. Fu, S. Wang, Y. Zhao, *Energy Environ. Sci.* **2021**, *14*, 1722.
- [20] a) M. A. Turov, P. V. Afanasiev, V. V. Lunin, *Appl. Catal. A* **1993**, *105*, 205; b) R. B. Patil, S. D. House, A. Mantri, J. C. Yang, J. R. McKone, *ACS Catal.* **2020**, *10*, 10390.
- [21] a) G. Dong, W. Ho, C. Wang, *J. Mater. Chem. A* **2015**, *3*, 23435; b) C. Lv, Y. Qian, C. Yan, Y. Ding, Y. Liu, G. Chen, G. Yu, *Angew. Chem., Int. Ed.* **2018**, *57*, 10246.
- [22] a) Y. Li, H. Zhang, M. Jiang, Y. Kuang, H. Wang, X. Sun, *J. Mater. Chem. A* **2016**, *4*, 13731; b) Y.-Y. Ma, C.-X. Wu, X.-J. Feng, H.-Q. Tan, L.-K. Yan, Y. Liu, Z.-H. Kang, E.-B. Wang, Y.-G. Li, *Energy Environ. Sci.* **2017**, *10*, 788; c) J. S. Li, Y. Wang, C. H. Liu, S. L. Li, Y. G. Wang, L. Z. Dong, Z. H. Dai, Y. F. Li, Y. Q. Lan, *Nat. Commun.* **2016**, *7*, 11204.
- [23] Q. Wang, X. Huang, Z. L. Zhao, M. Wang, B. Xiang, J. Li, Z. Feng, H. Xu, M. Gu, *J. Am. Chem. Soc.* **2020**, *142*, 7425.
- [24] H. Yan, Y. Xie, Y. Jiao, A. Wu, C. Tian, X. Zhang, L. Wang, H. Fu, *Adv. Mater.* **2018**, *30*, 1704156.
- [25] K. L. Zhou, Z. Wang, C. B. Han, X. Ke, C. Wang, Y. Jin, Q. Zhang, J. Liu, H. Wang, H. Yan, *Nat. Commun.* **2021**, *12*, 3783.
- [26] D. Chen, Z. Pu, R. Lu, P. Ji, P. Wang, J. Zhu, C. Lin, H. W. Li, X. Zhou, Z. Hu, F. Xia, J. Wu, S. Mu, *Adv. Energy Mater.* **2020**, *10*, 2000814.
- [27] X. Xiao, X. Wang, B. Li, X. Jiang, Y. Zhang, M. Li, S. Song, S. Chen, M. Wang, Y. Shen, Z. Ren, *Mater. Today Phys.* **2020**, *12*, 100182.
- [28] L. Li, B. Wang, G. Zhang, G. Yang, T. Yang, S. Yang, S. Yang, *Adv. Energy Mater.* **2020**, *10*, 2001600.
- [29] G. Chen, T. Wang, J. Zhang, P. Liu, H. Sun, X. Zhuang, M. Chen, X. Feng, *Adv. Mater.* **2018**, *30*, 1706279.
- [30] N. T. Suen, S. F. Hung, Q. Quan, N. Zhang, Y. J. Xu, H. M. Chen, *Chem. Soc. Rev.* **2017**, *46*, 337.
- [31] a) S. Yan, K. P. Abhilash, L. Tang, M. Yang, Y. Ma, Q. Xia, Q. Guo, H. Xia, *Small* **2019**, *15*, 1804371; b) M. Fang, D. Han, W. B. Xu, Y. Shen, Y. Lu, P. Cao, S. Han, W. Xu, D. Zhu, W. Liu, J. C. Ho, *Adv. Energy Mater.* **2020**, *10*, 2001059.
- [32] a) Y. Yang, L. Dang, M. J. Shearer, H. Sheng, W. Li, J. Chen, P. Xiao, Y. Zhang, R. J. Hamers, S. Jin, *Adv. Energy Mater.* **2018**, *8*, 1703189; b) C. Wei, S. Sun, D. Mandler, X. Wang, S. Z. Qiao, Z. J. Xu, *Chem. Soc. Rev.* **2019**, *48*, 2518.
- [33] S. Kozuch, J. M. L. Martin, *ACS Catal.* **2012**, *2*, 2787.
- [34] a) D. Fernandez, P. Maurer, M. Martine, J. M. Coey, M. E. Mobius, *Langmuir* **2014**, *30*, 13065; b) K. Dastafkan, Q. Meyer, X. Chen, C. Zhao, *Small* **2020**, *16*, 2002412.
- [35] C.-T. Dinh, A. Jain, F. P. G. de Arquer, P. De Luna, J. Li, N. Wang, X. Zheng, J. Cai, B. Z. Gregory, O. Voznyy, B. Zhang, M. Liu, D. Sinton, E. J. Crumlin, E. H. Sargent, *Nat. Energy* **2019**, *4*, 107.

- [36] a) Y. Yao, Y. Zhu, C. Pan, C. Wang, S. Hu, W. Xiao, X. Chi, Y. Fang, J. Yang, H. Deng, S. Xiao, J. Li, Z. Luo, Y. Guo, *J. Am. Chem. Soc.* **2021**, *143*, 8720; b) X. Li, X. Yang, L. Liu, H. Zhao, Y. Li, H. Zhu, Y. Chen, S. Guo, Y. Liu, Q. Tan, G. Wu, *ACS Catal.* **2021**, *11*, 7450.
- [37] a) Y. Jiang, Y. Song, Y. Li, W. Tian, Z. Pan, P. Yang, Y. Li, Q. Gu, L. Hu, *ACS Appl. Mater. Interfaces* **2017**, *9*, 37645; b) H. Zhao, Y. Mao, X. Mao, X. Shi, C. Xu, C. Wang, S. Zhang, D. Zhou, *Adv. Funct. Mater.* **2017**, *28*, 1704855.
- [38] E. Skúlason, V. Tripkovic, M. E. Björketun, S. Gudmundsdóttir, G. Karlberg, J. Rossmeisl, T. Bligaard, H. Jónsson, J. K. Nørskov, *J. Phys. Chem. C* **2010**, *114*, 18182.
- [39] R. Subbaraman, D. Tripkovic, D. Strmcnik, K.-C. Chang, M. Uchimura, A. P. Paulikas, V. Stamenkovic, N. M. Markovic, *Science* **2011**, *334*, 1256.
- [40] S. Song, L. Yu, X. Xiao, Z. Qin, W. Zhang, D. Wang, J. Bao, H. Zhou, Q. Zhang, S. Chen, Z. Ren, *Mater. Today Phys.* **2020**, *13*, 100216.